Supplementary Materials for

Tunable topological polaritons by dispersion tailoring of an active metasurface

Shaojie Wang, Ke Chen,* Shufang Dong, Tian Jiang, Junming Zhao and Yijun Feng*

Corresponding author: ke.chen@nju.edu.cn; yjfeng@nju.edu.cn

The file includes:

Sections S1 to S13

Figs. S1 to S20

Supplementary Information Guide:

Section S1. Equivalent circuit models of the unit cell

To gain an insight into the topological reconfigurable polaritons, we have established the effective circuit models of the proposed unit cell when the polaritons propagate along the *x* and *y* directions. The spoof surface plasma frequencies f_x and f_y can be derived as:

$$f_x = \frac{1}{2\pi}\sqrt{\frac{1}{L_{x1}}\cdot\frac{1}{C_{x1}+C_{x2}}}\cdot\sqrt{1+\frac{2\cdot(C_{x1}+C_{x2})\cdot C_{xh}+C_{x2}^{\ 2}}{C_{x1}\cdot C_{x2}+(C_{x1}+C_{x2})\cdot(C_{xh}+C_{xg}+C_v)}} \quad (1)$$

$$f_y = \frac{1}{2\pi}\sqrt{\frac{1}{L_{y1}}\cdot\frac{1}{C_{y1}+C_{y2}}}\cdot\sqrt{1+\frac{2\cdot(C_{y1}+C_{y2})\cdot C_{yh}+C_{y2}^{\ 2}}{C_{y1}\cdot C_{y2}+(C_{y1}+C_{y2})\cdot(C_{yh}+C_{yg}+C_v)}} \quad (2)$$

here C_{x1} and L_{x1} are the capacitance and inductance inside the top layer of the unit cell, C_{x2} comes from the mutual capacitance of the etching groove between the adjacent unit cells, C_{xh} is the grounded capacitance between top and bottom layers, C_{xg} originates from the complementary rectangle-shaped ring of bottom layer, and particularly, C_v is the intentionally introduced tunable capacitive load (**Figure S1**a,b), which are marked in **Figure S1**. The f_x and f_y are different from each other due to the anisotropy of the unit cell. Generally, the polaritons can propagate along both the *x* and *y* directions with the closed-elliptical topology of IFCs when $f_0 < f_x < f_y$, f_0 represents the operational frequency here, i.e., 6.1 GHz in the main text. In addition to this, polaritons propagating along the *x* direction will be no longer in existence if $f_x < f_0 < f_y$, and the topology of IFCs could be open ellipse, flat line, or hyperbola. Therefore, we are able to tailor the topology of polariton dispersions by altering the spoof surface plasma frequencies f_x and f_y. As for the proposed unit cell with fixed geometry parameters, the capacitances [C_{x1}

(C_{y1}), C_{x2} (C_{y2}), C_{xh} (C_{yh}) and C_{xg} (C_{yg})] and inductance [L_{x1} (L_{y1})] will keep constant while the loaded capacitances C_v possess the electrical tunability, hence the f_x and f_y will vary as the monotone function of C_v according to the equation (1) and (2), namely, we can obtain the controllable resonance frequencies along with continuously decreasing (increasing) loaded capacitances.

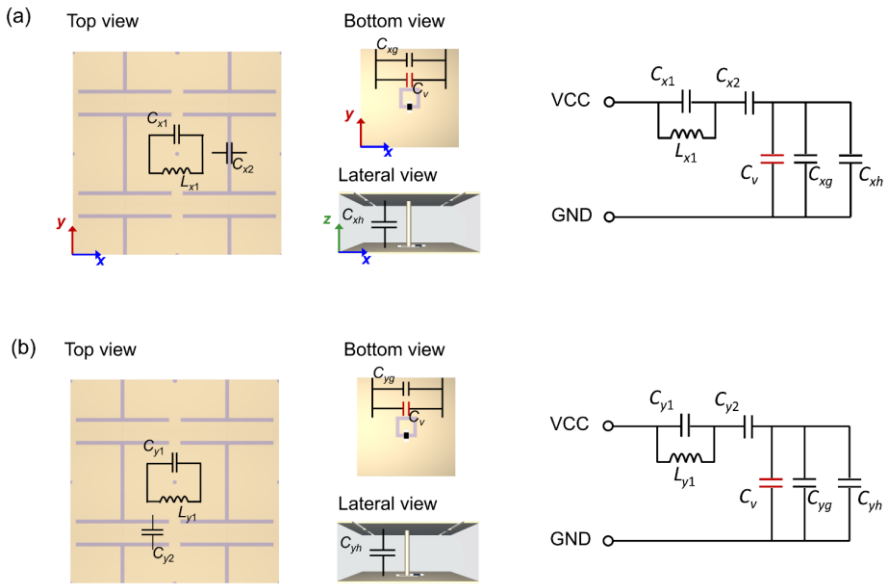

Figure S1. Equivalent circuit models of the proposed unit cell when designer polaritons propagate along the (a) *x* and (b) *y* directions, respectively.

We get the values of effective lumped capacitances and inductances when the polaritons propagate along the *x* and *y* directions by applying an equivalent circuit models-based retrieval process. As shown in **Figure S2**a,b, red and blue dotted lines represent simulated f_x and f_y using the eigenvalue module of a commercial software Computer Simulation Technology Microwave Studio. Blue square and red circular marks are calculated f_x and f_y by equivalent circuit models. Both f_x and f_y behave decreasing values along with increasing loaded capacitances. The calculated and simulated results match well with each other. Approximate values of the

equivalent lumped elements corresponding to **Figure S1** are C_{x1} = 0.1 pF, C_{x2}= 4 pF, C_{xh}= 0.4 pF, C_{xg}= 0.05 pF, L_{x1} = 1.8 nH and C_{y1} = 0.1 pF, C_{y2}= 2.4 pF, C_{yh}= 0.12 pF, C_{yg}= 0.04 pF, L_{y1} = 1.4 nH.

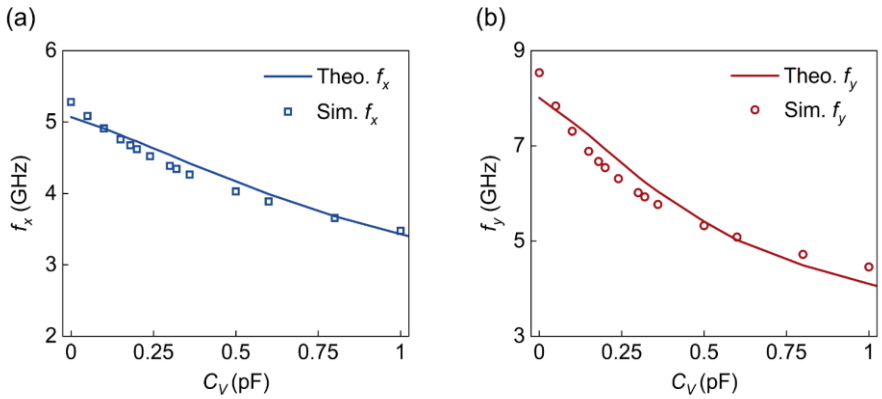

Figure S2. Simulated and theoretically calculated spoof surface plasma frequencies (a) f_x and (b) f_y as the function of loaded capacitances C_v when polaritons propagate along the x and y directions, respectively.

Section S2. Surface current distributions of the unit cell

The surface current distributions of the unit cells with different loaded capacitances are shown in **Figure S3**. Obviously, the reconfigurable metasurface manipulates the polaritons along the x and y propagating directions in different ways. The surface current distributions also show that the gap-induced capacitances between the adjacent unit cells and loaded capacitances of the varactor diodes play key roles in equivalent circuit models.

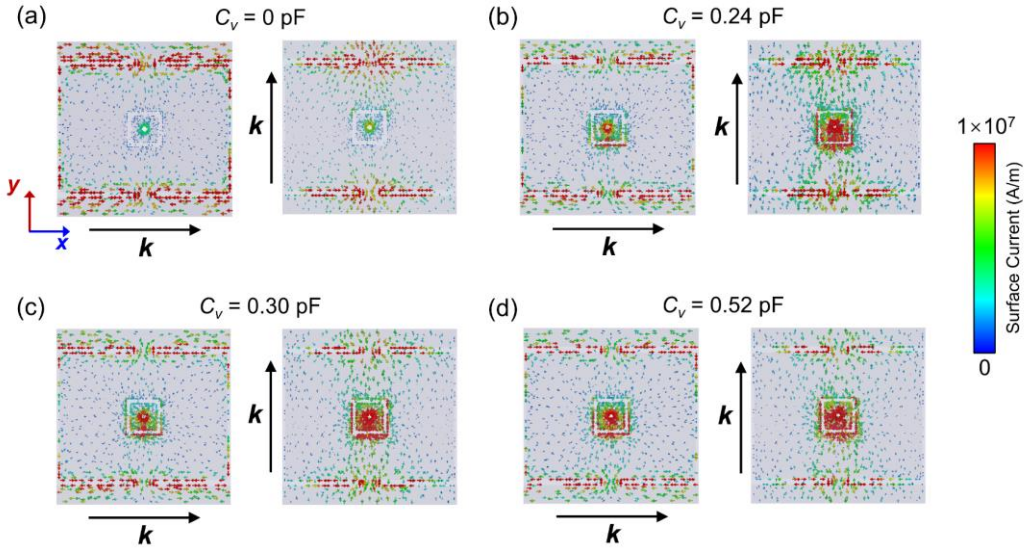

Figure S3. Surface current distributions of the unit cell when polaritons propagate the *x* and *y* directions, where the loaded capacitances are (a) 0 pF, (b) 0.24 pF, (c) 0.3 pF and (d) 0.52 pF, respectively.

Section S3. The details about the setting for numerical simulations

Dispersion characteristics of the designer polaritons in reconfigurable HM in the first Brillouin zone were numerically simulated by sweeping the phase based on the eigenvalue module of a commercial software CST Microwave Studio. The periodic boundary is set in the x and y directions, while the electric (E_t = 0) boundary is set in the z direction with around half-wavelength air above and below the unit cell. The eigen-frequencies obtained from CST will be used to get the band dispersions. The electric field distributions of the reconfigurable HM were simulated by full-wave simulations based on the Time Domain Solver. To efficiently excite the designer polaritons, a dipole source is put between the two metal layers of the unit cell located at the bottom edge of the metasurface. We monitor the field distributions in the *xy* plane that is 7 mm above the proposed reconfigurable metasurface, which is then used as the

input of a fast Fourier transform (FFT) to extract the IFCs. Additionally, the adopted varactor diode is modeled as an RLC series circuit.

Section S4. IFCs of the designer polaritons of the second band in the first Brillouin zone

We here give more information about the dispersion properties of the proposed meta-atom with the loaded capacitances of 0.52 pF. As shown in **Figure S4**a,b (mode 1), the spoof surface plasma frequencies of f_x (4.13 GHz) and f_y (5.33 GHz) are lower than 6.1 GHz, which denotes that the IFCs of the first band in the first Brillouin zone no longer exists at this frequency. Consequently, we carry out numerical simulations to obtain the dispersion properties of the second band (mode 2) in the first Brillouin zone. The dispersions diagrams of the second band (mode 2) in the first Brillouin zone when polaritons propagate along the x and y directions are shown in **Figure S4**a,b (mode 2), with the spoof surface plasma frequencies of f_x = 8.07 GHz and f_y = 9.94 GHz. Additionally, the polariton IFCs of the second band in the first Brillouin zone at different frequencies are shown in **Figure S4**c, where the polariton IFC behaves as a circle topology corresponding to the last panel in **Figure 2**a in the main text.

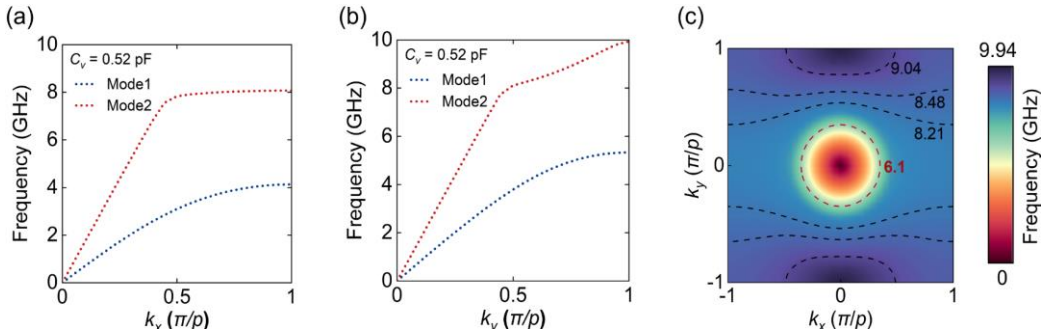

Figure S4. Dispersion diagrams of the first band (mode 1) and second band (mode 2) in the first Brillouin zone when polaritons propagate along the (a) *x* and (b) *y* directions with loaded capacitance of 0.52 pF. (c) IFCs of the second band in the first Brillouin zone at different frequencies with loaded capacitances of 0.52 pF.

Section S5. Dispersion equation based on anisotropic conductivity of the metasurface

To further reveal the conditions for realizing different topologies, we calculated the IFCs of the polaritons and provided relevant discussion. The conductivity of the proposed anisotropic unit cell can be generally modeled as a uniaxial surface conductivity tensor as the following:

$$\overline{\overline{\sigma}} = \begin{pmatrix} \sigma_{xx} & 0 \\ 0 & \sigma_{yy} \end{pmatrix}. \tag{1}$$

Besides, the dispersion equation for the TM surface wave has been proposed and can be compactly written as[17, 18]:

$$\eta_0^2(k_x^2\sigma_{xx} + k_y^2\sigma_{yy})^2(k_x^2 + k_y^2 - k_0^2) + 4k_0^2(k_x^2 + k_y^2)^2 = 0\,, \tag{2}$$

which can be adopted to describe the anisotropic hyperbolic metasurface effectively. The k_x and k_y represent the wave vectors of the polaritons propagating along x and y directions respectively, and k_0 is the wave vector in free space. Unfortunately, it's difficult to extract the equivalent

surface conductivity tensor of the proposed unit cell analytically. However, for the analysis of underlying physical mechanisms, the equivalent surface conductivity tensor can be retrived through the eq. (2) by comparing the calculated IFCs of the polaritons (solid curves in **Figure S5**a-d) and numerically simulated ones (dashed curves in **Figure S5**a-d). Then, the rationality of the retrieved equivalent surface conductivity tensor can be analyzed.

The comparison of calculated and simulated IFCs for different topologies are shown in **Figure S5**a to d, respectively, and the corresponding conductivity is σ_{xx} = 1+0.6i mS/m and σ_{yy} = 1+1.5i mS/m (**Figure S5**a), σ_{xx} = 0. 85+0. 48i mS/m and σ_{yy} = 0. 8+1.2i mS/m (**Figure S5**b), σ_{xx} = 0. 598+0.116i mS/m and σ_{yy} = 1.3-1.2i mS/m (**Figure S5**c), σ_{xx} = 2.1+3.3i mS/m and σ_{yy} = 2.1+3.3i mS/m (**Figure S5**d). As we have claimed in the main text the various polariton topologies arise depending on the specific constitutive parameter conditions of the anisotropic surface. Here, an inductive surface with positive imaginary part of both orthogonal conductivity components [Im(σ_{xx})>0 and Im(σ_{yy}) >0] can support elliptical topology corresponding to **Figure S5**a (Im(σ_{xx}) = 0.6 mS/m, Im(σ_{yy}) = 1.5 mS/m and sgn[Im(σ_{xx})] · sgn[Im(σ_{yy})] > 0), **Figure S5**b (Im(σ_{xx}) = 0.48 mS/m, Im(σ_{yy}) = 1.2 mS/m and sgn[Im(σ_{xx})] · sgn[Im(σ_{yy})] > 0) and **Figure S5**d (Im(σ_{xx}) = Im(σ_{yy}) = 3.3 mS/m and sgn[Im(σ_{xx})] · sgn[Im(σ_{yy})] > 0). By manipulating the strong in-plane anisotropy of the metasurface based on the controllable capacitances of the electrically driven varactor diode, the polaritons dispersion can be tailored. As expected, hyperbolic dispersion topology arises when the surface behaves as inductive and capacitive one along the

orthogonal direction respectively, corresponding to **Figure S5**c ($\mathrm{Im}(\sigma_{xx})$ = 0.116 mS/m, $\mathrm{Im}(\sigma_{yy})$ = -1.2 mS/m and $\mathrm{sgn}[\mathrm{Im}(\sigma_{xx})] \cdot \mathrm{sgn}[\mathrm{Im}(\sigma_{yy})] < 0$).

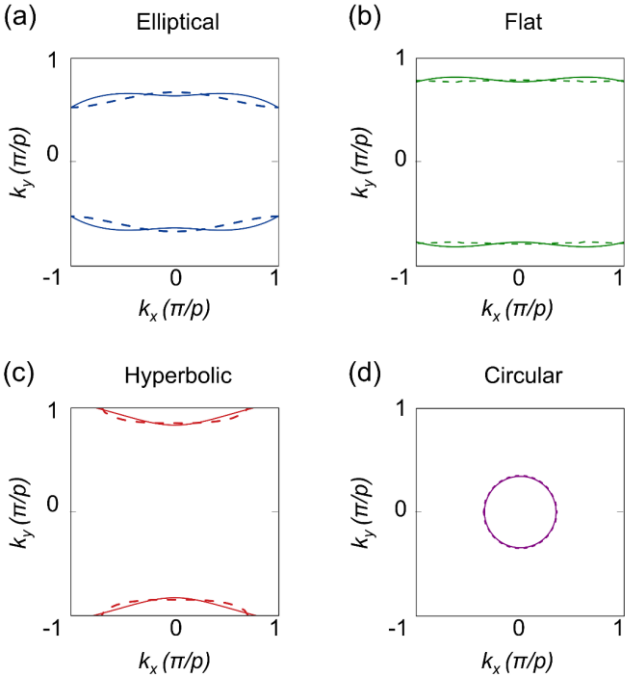

Figure S5. Calculated and simulated iso-frequency contours for (a) elliptical, (b) flat, (c) hyperbolic, and (d) circular topologies, where the solid curves and dashed curves represent the calculated and simulated ones, respectively.

Section S6. The capacitance of the varactor as a function of the bias voltage

Here, the calculation function between the capacitance of the varactor and the bias voltage is plotted in **Figure S6**. The calculation function is extracted from experimental measurements.[57] Besides, the capacitances of the varactor under typical bias voltages are also provided in **Table. S1**."

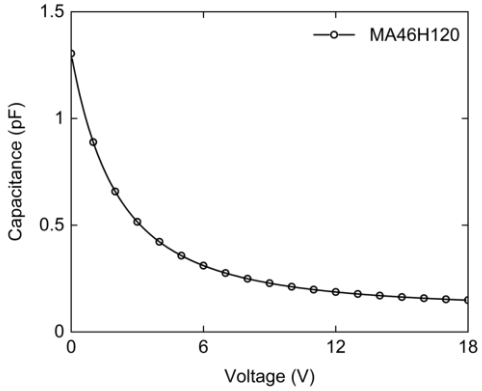

Figure S6. Series capacitance of the varactor as a function of the bias voltage.

Table S1. Capacitances C_v (pF) of the varactor under different bias voltages V_C (V)

V_C	C_v	V_C	C_v	V_C	C_v
0	1.30	4.5	0.39	8.5	0.24
1	0.89	5	0.36	9	0.23
1.5	0.76	5.5	0.33	9.5	0.22
2	0.66	6	0.31	10	0.21
2.5	0.58	6.5	0.29	10.5	0.20
3	0.52	7	0.28	11	0.20
3.5	0.46	7.5	0.26	11.5	0.19
4	0.42	8	0.25	12	0.19

Section S7. The Experimental measurements on the response time of the topology switching

Additional measurements have been conducted to evaluate the switching speed of the topology transition with the adopted varactor diodes based on the experimental setup shown in **Figure S7**. The samples were placed on a 3D movement platform, as shown in **Figure 2d**. Take

the operation frequency of 5.5 GHz as an example, the biased voltage is tuned to be a square wave that allows the metasurface to support the suppression of polariton propagation at 0 V and field canalization at 5 V (shown in **Figure S10**), respectively. A monopole antenna is used to detect the modulating signal. The received transient signal will be switched between high- and low-level, namely corresponding to the working state of polariton propagation suppression and non-diffraction propagation. Thus, one can find the switching speed by observing the waveforms of the received modulating signal. The real-time measured results for the square wave with different modulation frequency f_m from 50 KHz to 20 MHz are shown in the following **Figure S8**a to i. The detected results are standard square waveforms with the same frequency for the modulation frequency of 50 KHz and 100 KHz. Here, the orange dashed and dotted lines represent the high- and low-level in a modulation signal cycle, respectively. As the modulation frequency increases to 300 KHz, the detected modulation signal witnesses certain waveform deterioration, but still with the obvious high- and low-level in a signal cycle, being identical to that of orange dashed and dotted lines in **Figure S8**a. Further increasing the modulation frequency to 400 KHz and 1 MHz will result in a distorted waveform with inaccurate high- and low-level, indicating the reconfigurable metasurface cannot effectively respond to the modulation frequency. Moreover, the detected modulating signal degrades to an obvious triangular waveform when it comes to the modulation frequency larger than 10MHz. Consequently, the efficient switching speed for the adopted varactor diode corresponds to 300

KHz modulation at least. It should be noted that there are two switches in a modulation signal circle, hence it indicates a switching time of 1/(300K×2) = 1.6 μs or 6×10^5 switches per second.

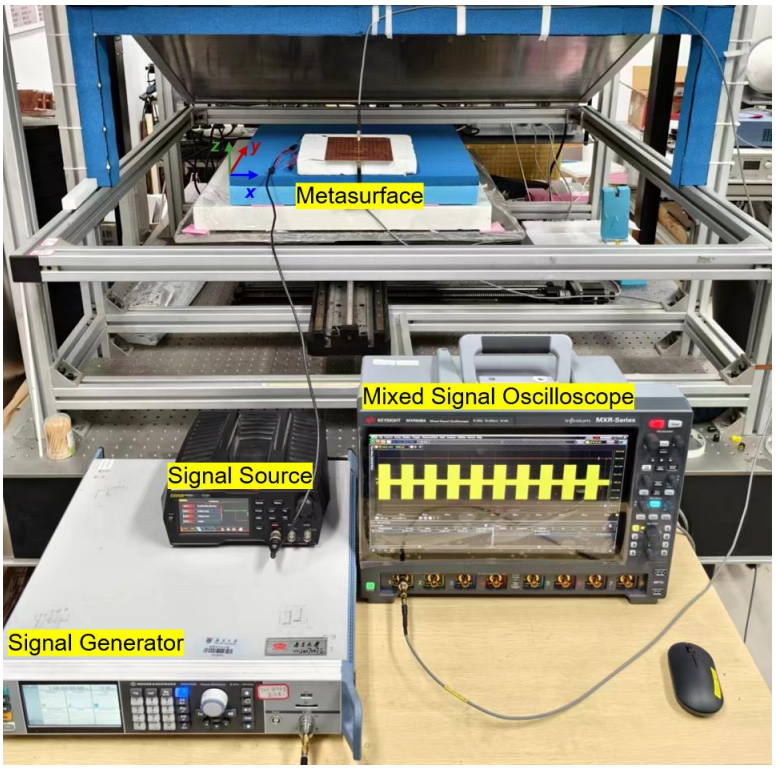

Figure S7. Photograph of the experimental setup for the measurement of the switching speed of the topology transition with the adopted varactor diodes (type MA46H120). The used instruments shown in the photograph are Signal Source (type RIGOL DG992 100 MHz), Signal Generator (type ROHDE & SCHWARZ SMA100B 8 KHz - 20 GHz), and Mixed Signal Oscilloscope (KEYSIGHT MXR608A 6 GHz).

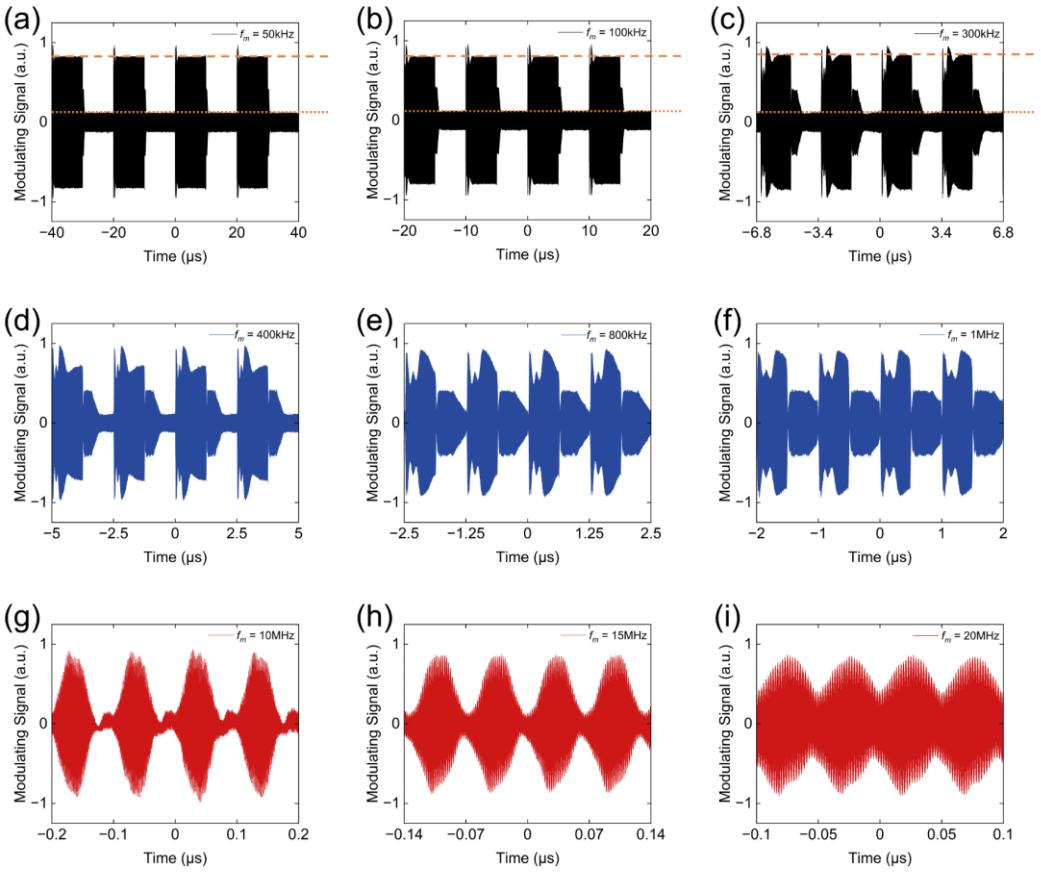

Figure S8. The real-time modulating signal variation measured in the *xy* plane that is 1 mm above the proposed reconfigurable metasurface with different modulation frequency f_m of (a) 50 KHz, (b) 100 KHz, (c) 300 KHz, (d) 400 KHz, (e) 800 KHz, (f) 1 MHz, (g) 10 MHz, (h) 15 MHz and (i) 20 MHz. The adopted carrier frequency is 5.5 GHz.

Section S8. Simulated and measured results for controllable field canalization

In this section, we provide more results to demonstrate the flexibly controllable field canalization based on the proposed reconfigurable HM, including simulated results ranging from 5.9 GHz to 6.3 GHz, and measured results ranging from 5.5 GHz to 6.3 GHz corresponding to the green circles in **Figure 3**a in the main text, as shown in **Figure S9** and **Figure S10**, respectively. The metasurface consists of 24×16 unit cells with a size of 204×136 mm^2. Both simulations and measurements fully validate the feasibility of electrically controllable field canalization.

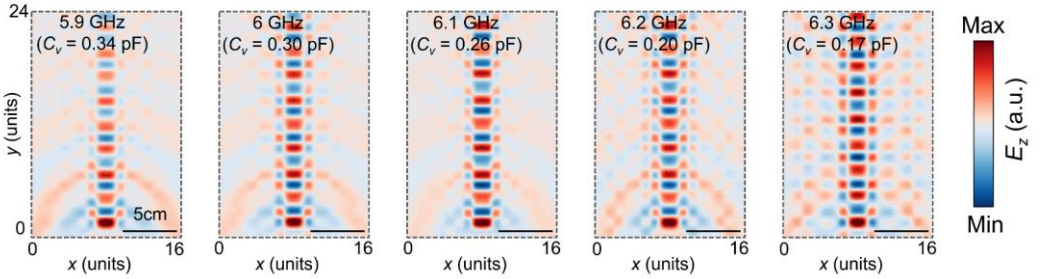

Figure S9. Simulated field distributions [Re (E_z)] in the *xy* plane that is 7 mm above the reconfigurable HM at 5.9 GHz (C_v = 0.34 pF), 6 GHz (C_v = 0.30 pF), 6.1 GHz (C_v = 0.26 pF) and 6.2 GHz (C_v = 0.20 pF) and 6.3 GHz (C_v = 0.17 pF). The observation areas consist of 24×16 unit cells with a size of 204×136 mm^2. The abbreviation a.u. represents arbitrary units.

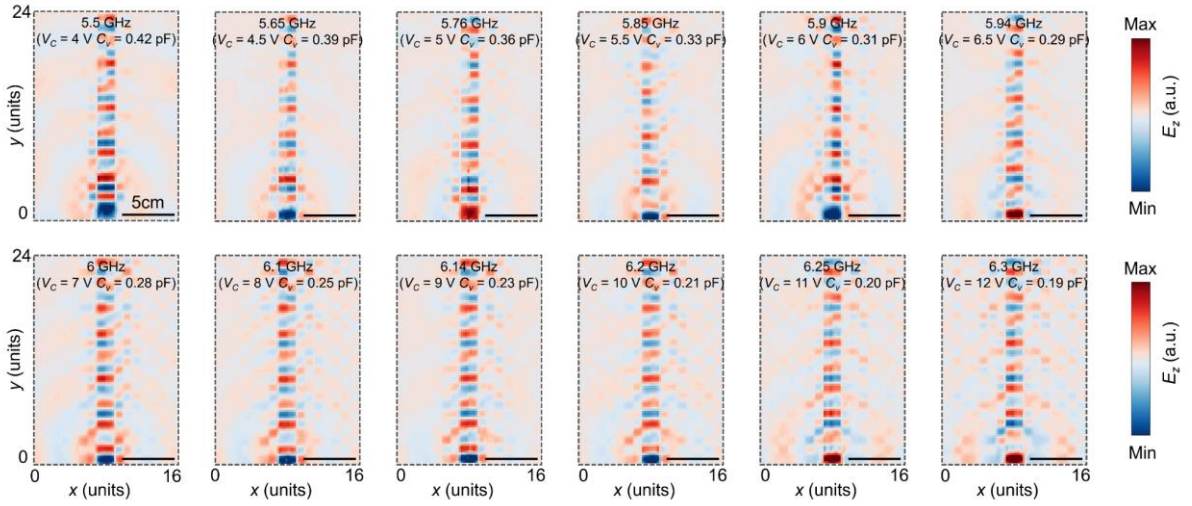

Figure S10. Measured field distributions [Re (E_z)] in the *xy* plane that is 1 mm above the reconfigurable HM at different frequencies. The observation areas consist of 24×16 unit cells with a size of 204×136 mm^2.

It is worth mentioning that the phenomenon of field canalization can also be observed by optionally changing the positions of excitation sources thanks to the global dispersion control characteristic. As shown in **Figure S11**, the dipole sources are placed on the left (**Figure S11**a) and right sides (**Figure S11**b) at the bottom side of the metasurface respectively, and the designer polaritons can propagate in a self-collimating manner in both cases. Moreover, the polariton propagates in two different channels can be realized by simultaneously placing two excitation sources at the corresponding positions. These results further illustrated the potential of the proposed metasurface in designing spatial multiplexers with applications in multi-channel near-field information processing.

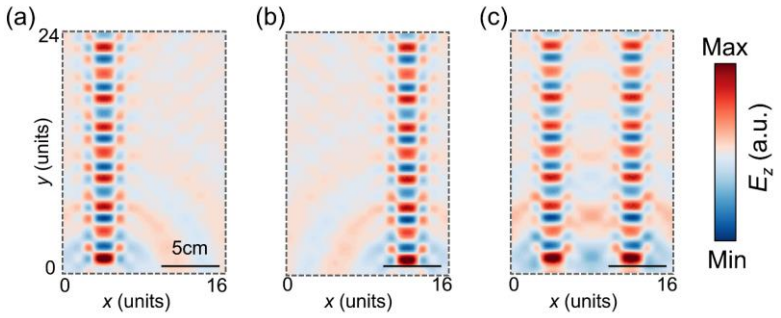

Figure S11. Simulated field distributions [Re (E_z)] in the *xy* plane that is 7 mm above the reconfigurable HM at 6.1 GHz (C_v = 0.26 pF) with excitation sources located at different positions, corresponding to (a) fifth unit cell from left, (b) fifth unit cell from right sides and (c) dual positions at the bottom side of the metasurface.

Section S9. The discussion of the propagation loss of the polaritons

Without loss of generality, here, we discuss the loss/propagation distance of the polariton by taking the field canalization as an instance. Several kinds of metasurfaces with different loss characteristics have been investigated, including the lossless metasurface, the metasurface with lossy dielectric and metal (copper), and the metasurface with parasitic resistance (2 Ω) of loaded varactor diode. For the lossless metasurface, the dielectric is assumed lossless and the metal a perfect electric conductor (PEC), while realistic F4B substrate (tangential loss tanδ = 0.001) and copper (conductivity $\sigma = 5.96\times10^7$ S/m) is adopted for the metasurface with lossy dielectric and metal, but the parasitic resistance is set as 0 Ω for the later one. The excitation source is placed at the bottom side of the metasurface, and the simulated field distributions [Re (E_z)] are demonstrated in **Figure S12**.

Increasing loss can decrease the amplitude of the polaritons at the identical propagation

distance. Then, the electric field amplitude ($|E_z|$) and phase profiles along the y-axis, passing through the center in the *xy* plane that is 7 mm above the metasurfaces are extracted and presented in **Figure S13**, including the results for lossless metasurface (**Figure S13**a,b), the one with lossy dielectric and metal (**Figure S13**c,d), and the one with parasitic resistance of 2 Ω (**Figure S13**e,f). Particularly, the strong reflections at the boundary of the metasurfaces result in the amplitude oscillation of the polaritons. Generally, the amplitude of the polaritons needs to satisfy an exponential decaying tendency with the increasing propagation length. Hence the propagation loss function of the polariton modes that increase as the propagation length increases could be fitted through the simulated amplitude peaks when the polaritons are propagating steadily. The above fitting functions are plotted and demonstrated in **Figure S13**a,c,e with dashed curves. As expected, the polariton can continue to propagate with almost no loss for the lossless metasurface, and the amplitude attenuation is also not obvious for the metasurface with only dielectric and metal loss. Nevertheless, the amplitude attenuation is much more obvious when considering the parasitic resistance. The attenuation length α could be calculated at around 4.2 λ. Here, the attenuation length α is defined as the propagation distance where the amplitude of polariton drops to 1/e (e is the Euler's number of 2.718). Thus, for the varactor diodes adopted in the work (with a parasitic resistance of around 2 Ω), the amplitude of the polaritons will drop to 1/e at the propagation length of around 4.2 λ according to the above results.

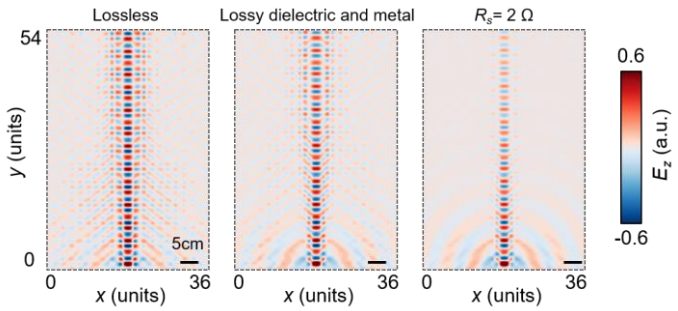

Figure S12. Simulated field distributions [Re (E_z)] in the *xy* plane that is 7 mm above the reconfigurable metasurface at 6.1 GHz for metasurfaces with different loss characteristics. The observation areas consist of 54×36 unit cells with a size of 459×306 mm^2.

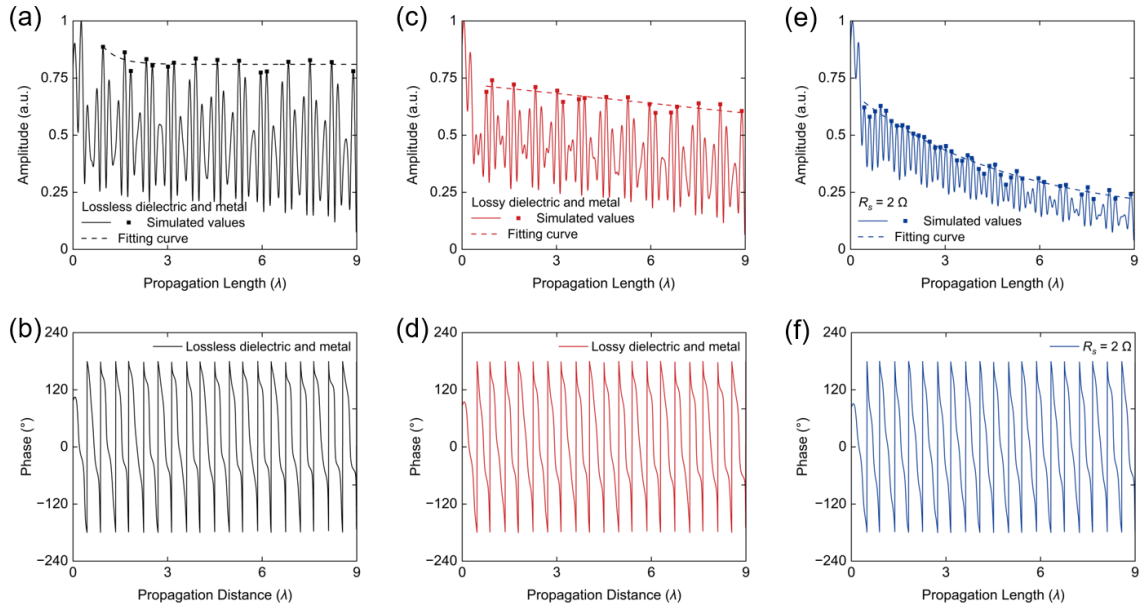

Figure S13. Normalized simulated electric field profile along the y-axis, passing through the center in the *xy* plane that is 7 mm above the metasurface. (a) Amplitude ($|E_z|$) and (b) phase profile for lossless metasurface, (b) amplitude ($|E_z|$) and (c) phase profile for metasurface with lossy dielectric and copper, (e) amplitude ($|E_z|$) and (f) phase profile for metasurface with parasitic resistance (2 Ω) of loaded varactor diodes. The abbreviation a.u. represents arbitrary units.

Section S10. Simulated and measured results for tunable planar focusing

In this part, we also provide more results for tunable planar focusing functionality based on the same reconfigurable HM as that in Section S8, including simulated results ranging from 6.1

GHz to 6.5 GHz, and measured results ranging from 6.04 GHz to 6.6 GHz, as shown in **Figure S14** and **Figure S15**, respectively. The observation areas have a size of 136×136 mm^2. Polariton IFC can be continuously switched to a hyperbola over certain frequency bands by applying a different bias voltage, leading to the tunable planar focusing. Excellent performances can be observed in both simulations (**Figure S14**) and measurements (**Figure S15**), where the EM energy is stably focused into a hotspot in the surrounding air medium.

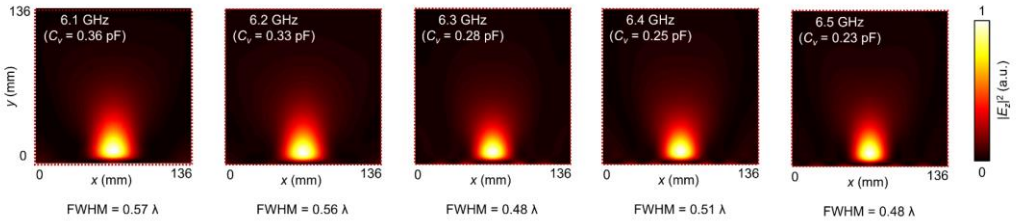

Figure S14. Simulated intensity distributions ($|E_z|^2$) in the *xy* plane that is 7 mm above the reconfigurable HM at 6.1 GHz (C_v = 0.36 pF), 6.2 GHz (C_v = 0.33 pF), 6.3 GHz (C_v = 0.28 pF) and 6.4 GHz (C_v = 0.25 pF) and 6.5 GHz (C_v = 0.23 pF). The observation areas have a size of 136×136 mm^2.

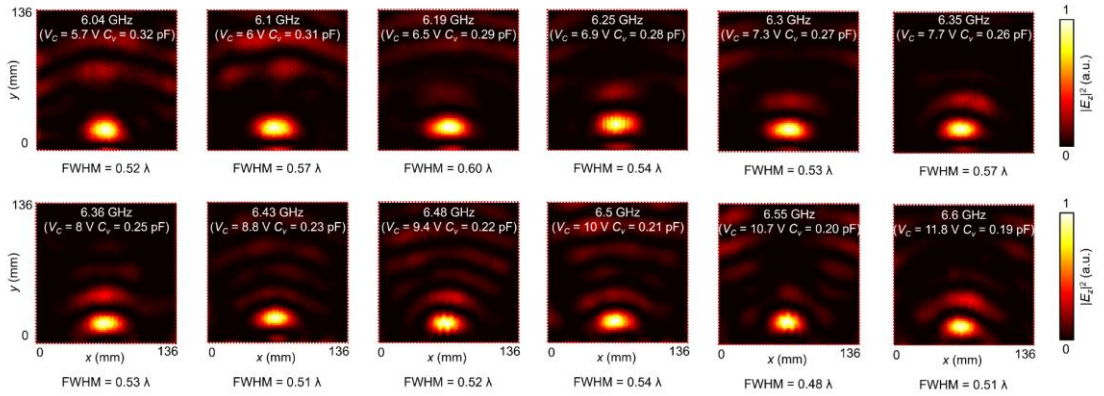

Figure S15 Measured intensity distributions ($|E_z|^2$) in the *xy* plane that is 1 mm above the reconfigurable HM at different frequencies. The observation areas have a size of 136×136 mm^2.

Section S11. Other functionalities of reconfigurable integrated polariton circuit

To further demonstrate the flexibility of the proposed planar reconfigurable polariton circuits for polariton manipulation, other functionalities are shown below. The collimating refraction (**Figure S16**a) occurs at the interface when the polariton IFC is set to be flat dispersion in region 2 (see movie S8). However, the suppression of polariton propagation (**Figure S16**b) can be realized when the loaded capacitance in region 2 is set as a large value of 0.52 pF (see movie S9).

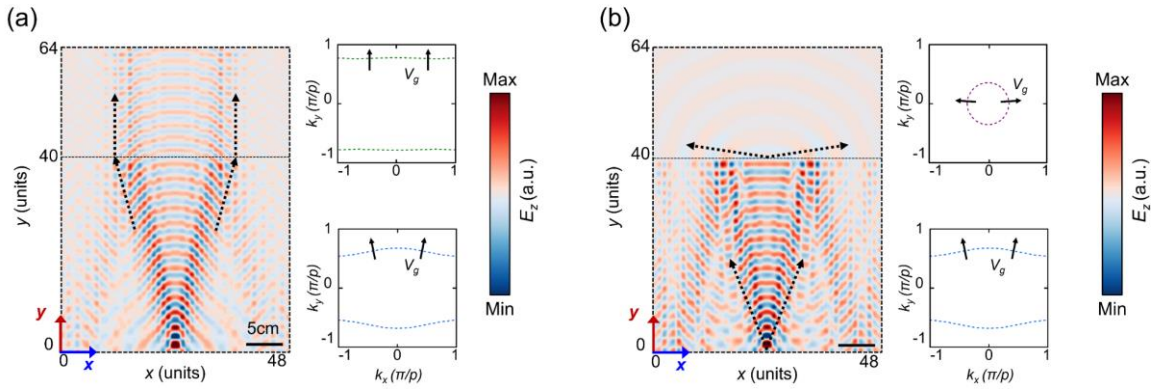

Figure S16. Simulated field distributions [Re (E_z)] in the *xy* plane that is 7 mm above the polariton circuit. The loaded capacitances in region 1 and region 2 are (a) 0.03 pF and 0.28 pF for collimating refraction and (b) 0.03 pF and 0.52 pF for suppression of polariton propagation, respectively.

Section S12. Reconfigurable integrated polariton circuit with four regions

The proposed metasurface can also realize extraordinary propagation phenomena of polaritons with a more complex combination of topologies of polariton dispersion. Here, a reconfigurable integrated polariton circuit with four regions is presented for multi-channel power allocation at the operation frequency of 5.3 GHz. We carry out numerical simulations to obtain the dispersion properties of the first band in the first Brillouin zone at the loaded capacitances of 0.03pF (upper panel of **Figure S17**a), and the second band in the first Brillouin zone at the loaded capacitances of 0.72pF (upper panel of **Figure S17**b). Additionally, the polariton IFCs of the first and second band in the first Brillouin zone at different frequencies are shown in the bottom panels of **Figure S17**a,b, where the polariton IFC behaves as an elliptical and a circular topology at 5.3GHz, respectively.

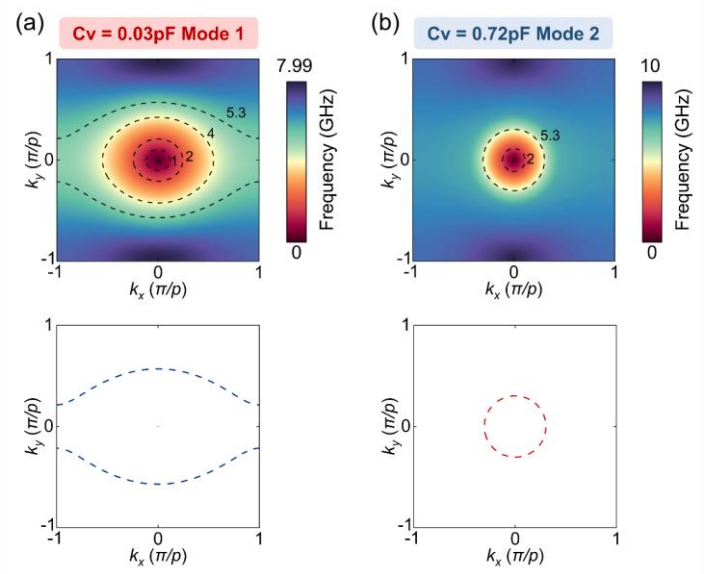

Figure S17. IFCs of the (a) first band and (b) second band in the first Brillouin at different frequencies with loaded capacitances of 0.03 pF and 0.72 pF respectively. The bottom panels

of (a) and (b) are elliptical and circular topologies of the IFC of the polaritons at the operational frequency of 5.3 GHz.

Figure S18a shows the schematic of the planar reconfigurable integrated polariton circuit with 4 regions, where orange, green, blue, and purple blocks denote the specific region, being similar to that in **Figure 4**a. It should be noted that the loaded capacitance of each region can choose between two values of 0.03 pF or 0.72 pF, which can be realized by applying different voltages on the corresponding regions. The polaritons propagation will be obviously suppressed at the regions with the loaded capacitance of 0.72 pF (corresponding to a circular topology), being similar to that in the last panel of **Figure 2**b). While at the regions with loaded capacitance of 0.03pF, the polaritons can effectively propagate with convex wavefront due to the elliptical dispersion. Hence, the on-demand manipulation and guidance of polaritons propagation can be engineered by tailoring the distributions of the topologies of polariton dispersions. **Figure S18**b-h provides the simulated field distributions above the polariton circuit for several representative cases, where the propagating directions of the polaritons can be manipulated effectively, with flexibility and diversity. The intriguing phenomenon may serve as an efficient platform and find potential application in surface power dividers. The distributions of topologies of polariton dispersions corresponding to **Figure S18**b-h are provided in **Table S2**."

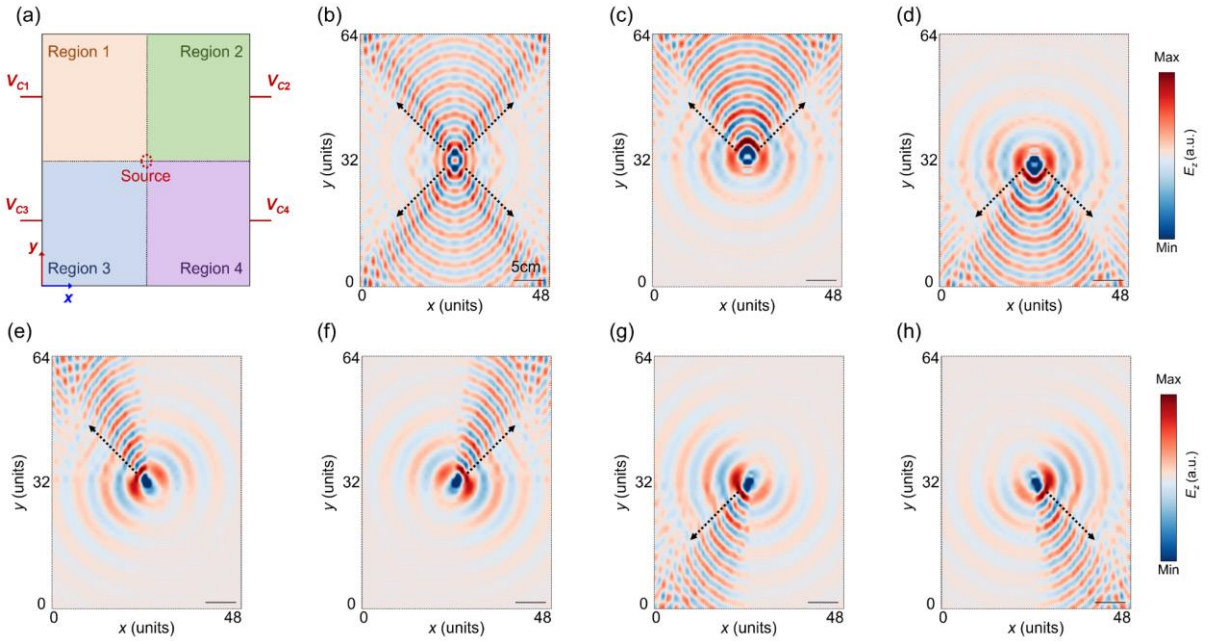

Figure S18. Reconfigurable integrated polariton circuit with potential application in surface wave multi-channel power divider. (a) Schematic of the planar reconfigurable polariton circuit composed of four regions (region 1 to region 4) represented by orange, green, blue, and purple blocks respectively. The loaded capacitances of unit cells are divided into four regions leading to different topologies of polariton dispersions, being similar to that in **Figure 4**a. The red dashed circle located in the center of the polariton circuit represents the excitation source. (b-h) Simulated field distributions [Re (E_z)] in the *xy* plane that is 7 mm above the polariton circuit at the operation frequency is 5.3 GHz. The dotted lines indicate the main propagating directions of the polaritons. The observation areas consist of 48×64-unit cells with a size of 408×544 mm^2.

Table S2. Constituent regions corresponding to **Figure S18**

	Region 1	Region 2	Region 3	Region 4
Figure S18b	Elliptical	Elliptical	Elliptical	Elliptical
Figure S18c	Elliptical	Elliptical	Circular	Circular
Figure S18d	Circular	Circular	Elliptical	Elliptical
Figure S18e	Elliptical	Circular	Circular	Circular
Figure S18f	Circular	Elliptical	Circular	Circular
Figure S18g	Circular	Circular	Elliptical	Circular
Figure S18h	Circular	Circular	Circular	Elliptical

* The loaded capacitances are 0.03pF and 0.72pF for elliptical and circular regions, respectively.

Section S13. Planar programmable integrated polariton circuit

As a representative demonstration, the concept of a planar programmable integrated polariton circuit with potential applications has been further proposed and demonstrated here to fully reveal the unique advantages of the methodology for active engineering of topological polaritons. We carry out numerical simulations to obtain the dispersion properties of the first band in the first Brillouin zone at the loaded capacitances of 0.12 pF (upper panel of **Figure S19**a), and the second band in the first Brillouin zone at the loaded capacitances of 0.72 pF (upper panel of **Figure S19**b). The corresponding polariton IFCs at different frequencies are shown in the bottom panels of **Figure S19**a,b, where the polariton IFC behaves as an elliptical and a circular topology state at 5.3 GHz, respectively. Similar to that in section S12, the polaritons propagation will be obviously suppressed at the regions with the loaded capacitance of 0.72 pF, while the polaritons can effectively propagate at the regions with the loaded capacitance of 0.12 pF.

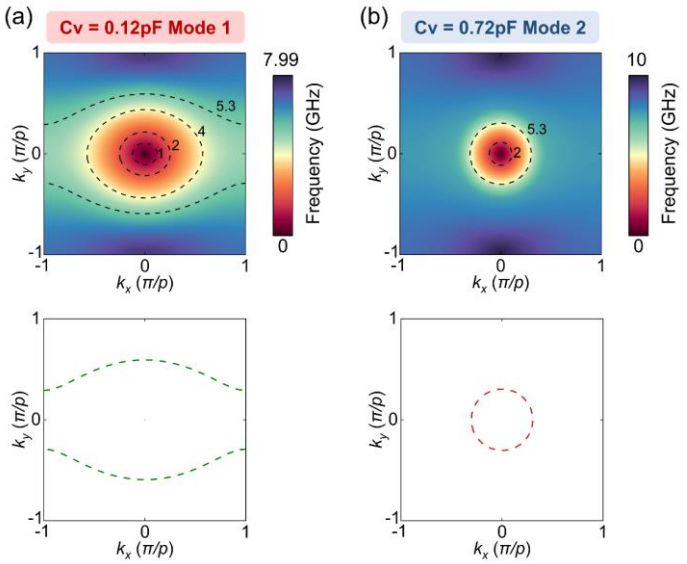

Figure S19. IFCs of the (a) first band and (b) second band in the first Brillouin at different frequencies with loaded capacitances of 0.12 pF and 0.72 pF respectively. The bottom panels of (a) and (b) are elliptical and circular topologies of the IFC of the polaritons at the operational frequency of 5.3 GHz.

Consider a metasurface composed of 36×18 unit cells, the loaded capacitance of each unit cell can be arbitrarily tuned to 0.72 pF or 0.12 pF, which are correspondingly defined as 0 state and 1 state respectively. Hence, we can tailor the distributions of the 0 and 1 states on the metasurface to be various shapes. For simplicity, consider that the 0 and 1 states on the metasurface are tailored as the distributions shown in the left panel of **Figure 20**a, and the excitation source is placed at the location of the first unit cell with 1 state at the left boundary of the metasurface. Then, the polaritons will be effectively excited and propagate on the metasurface. Once the polaritons propagate toward the unit cells with 0 state, the strong reflection occurs, while efficient propagation can be realized vice versa. The above EM responses are constrained based on the dispersion characteristics of the unit cell. Thus, the excited polaritons will constantly reflect and propagate in oscillations along the propagation

route defined by the unit cells with 1 state, which is verified by the simulated amplitude distributions of the polaritons, as shown in the right panel of **Figure 20**a. Then, a series of cases for polaritons guidance (covering multi-excitation sources, multi ports, and flexibly designable propagation routes) have been designed and simulated (**Figure S20**a-f). By dynamic local dispersion engineering based on a single reconfigurable metasurface, we present the 90° sharp bending waveguide, retroreflection waveguide, waveguide splitters, and multi-port waveguide, which significantly expanded the possibilities for manipulation of the polaritons propagation.

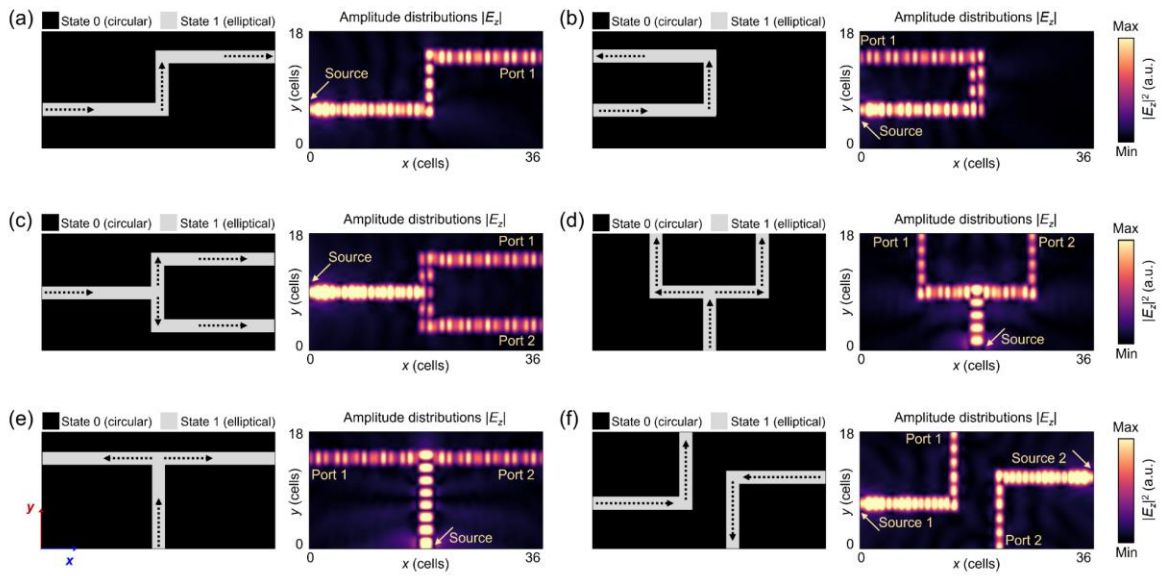

Figure S20. Planar programmable polariton circuit with potential application in surface wave waveguide. Left panels of (a) to (f) are the Schematic of the programmable polariton circuit composed of two kinds of unit cells denoted as state 0 and state 1 with circular and elliptical topology of polariton dispersions respectively. The loaded capacitances of unit cells are 0.72 pF and 0.12 pF respectively, thus leading to different EM responses of polariton dispersions. Right panels of (a) to (f) are simulated amplitude distributions ($|E_z|$) in the *xy* plane that is 7 mm above the programmable polariton circuit at the operation frequency is 5.3 GHz. The gold arrows in the right panels represent the excitation source. The dotted lines indicate the designed propagating directions of the polaritons. The observation areas consist of 36×18-unit cells with a size of 306×153 mm^2.